

# Development of ferroelectric domains and topological defects in vacancy doped ceramics of h-LuMnO<sub>3</sub>

A. Baghizadeh, J. M. Vieira, P. Mirzadeh Vaghefi, M.-G. Willinger, and V. S. Amaral

Citation: *Journal of Applied Physics* **122**, 044102 (2017); doi: 10.1063/1.4996349

View online: <http://dx.doi.org/10.1063/1.4996349>

View Table of Contents: <http://aip.scitation.org/toc/jap/122/4>

Published by the American Institute of Physics

---

---



The advertisement features the AIP logo in orange and yellow, followed by "Journal of Applied Physics". Below the logo, there is promotional text about publishing research for free. On the right side, there is a call to action to publish research in the journal.

**AIP | Journal of Applied Physics**

Save your money for your research.  
It's now **FREE** to publish with us -  
no page, color or publication charges apply.

Publish your research in the  
***Journal of Applied Physics***  
to claim your place in applied  
physics history.

# Development of ferroelectric domains and topological defects in vacancy doped ceramics of h-LuMnO<sub>3</sub>

A. Baghizadeh,<sup>1</sup> J. M. Vieira,<sup>1</sup> P. Mirzadeh Vaghefi,<sup>2</sup> M.-G. Willinger,<sup>3</sup> and V. S. Amaral<sup>2</sup>

<sup>1</sup>Department of Materials and Ceramic Engineering and CICECO, Aveiro University, 3810-193 Aveiro, Portugal

<sup>2</sup>Physics Department and CICECO, Aveiro University, Aveiro, Portugal

<sup>3</sup>Department of Inorganic Chemistry, Fritz Haber Institute of the Max Planck Society, Faradayweg 4-6, Berlin, Germany

(Received 16 December 2016; accepted 16 July 2017; published online 27 July 2017)

Self-doping of the h-LuMn<sub>x</sub>O<sub>3±δ</sub> ( $0.92 \leq x \leq 1.12$ ) phase and changes in the sintering time are applied to investigate the formation and annihilation of antiphase ferroelectric (FE) domains in bulk ceramics. The increase in the annealing time in sintering results in growth of FE domains, which depends on the type of vacancy, 6-fold vortices with dimensions of the order of 20 μm being observed. Interference of planar defects of the lattice with the growth of topological defects shows breaking of 6-fold symmetry in the self-doped ceramics. The role of grain boundaries in the development of topological defects has been studied. Dominance of the atypical FE domain network in very defective h-LuMn<sub>x</sub>O<sub>3±δ</sub> lattices saturated with Mn vacancies ( $x < 1$ ) was also identified in the current study. After a long annealing time, scattered closed-loops of nano-dimensions are often observed isolated inside large FE domains with opposite polarization. Restoring of the polarization after alternative poling with opposite electrical fields is observed in FE domains. Stress/strain in the lattice driven by either planar defects or chemical inhomogeneity results in FE polarization switching on the nanoscale and further formation of nano-vortices, with detailed investigation being carried out by electron microscopy. Pinning of FE domains to planar defects is explored in the present microscopy analysis, and nano-scale observation of lattices is used to explain features of the ferroelectricity revealed in Piezo Force Microscopy images of the ceramics. Published by AIP Publishing.

[<http://dx.doi.org/10.1063/1.4996349>]

## I. INTRODUCTION

Ferroelectricity of hexagonal h-RMnO<sub>3</sub> oxides presents strikingly new features of most relevance for this class of multiferroics as they show intrinsic interlocking of topological defects at anti-phase boundaries (APBs), with ferroelectric (FE) domain walls. The underlying physics of interlocking of FE domains with topological defects in the lattices of single crystals of h-RMnO<sub>3</sub> oxides is intensively investigated.<sup>1–6</sup> Recently, attention paid to patterns of APB-FE domain walls interacting with oxygen vacancies or point defects in the crystalline lattices of h-RMnO<sub>3</sub> oxides different from 6-fold vortex networks of stoichiometric composition created a better understanding of mutual interactions of lattice defects and FE domains in these oxides. Still, studies on the role of vacancies with effective electric charge, planar defects, and dislocations in the FE properties and formation of vortex/antivortex domain patterns in these oxides are rare.<sup>7,8</sup>

Evidence of the effects of Lu vacancies or Mn vacancies and extended defects of the crystalline lattice on FE domains of as-sintered h-LuMn<sub>x</sub>O<sub>3±δ</sub> ceramics will be presented in this paper. Cation vacancies of Mn ( $x < 1$ ) or Lu ( $x > 1$ ) are introduced by self-doping the h-RMnO<sub>3</sub> oxide as a means to alter the unit cell dimensions and perturb ion-to-ion interactions with shifts away from the stoichiometric composition. The evolution of FE domains and 6-fold vortices and the causes of topology breaking in self-doped ceramics were investigated by means of Piezo Force Microscopy (PFM)

and TEM/STEM analysis. The effects of annealing time as a parameter of the sintering process on the FE domain growth and rendering of 6-fold vortices were also studied. TEM analysis is used to reveal interactions of planar defects at the nano-scale or shifts of the elemental composition within FE domains. Dark-field TEM with lattice images taken around defective regions in the correct crystal orientation to project the displacement of Lu ions is employed to explain interactions of planar defects with shifting of the polarization switching/phase on domain walls.

## II. TOPOLOGICAL NETWORKS

The essential feature of topological FE domains in polar h-RMnO<sub>3</sub> is derived from their distribution around 6-fold vortices in space. As seen at room temperature, the core of each vortex in a complete 6-fold domain topology is the intersection of volumes of three anti-phase domains with  $2\pi/3$  phase shifts, with the direction of FE polarization being reversed when the vortex-core line is crossed inside the same anti-phase domain with an equal trimerization angle.<sup>2,3,9,10</sup> Vortex-core lines of complete 6-fold vortex networks in h-RMnO<sub>3</sub> perfect crystals are free to bend in single or multiple U-turns; they may even form closed-loops but never intersect together inside the crystal, with their free ends being found on crystal surfaces. On the same principle, nerves of several vortex-core lines of the set of APB-FE domain walls delimiting the volume of one given FE domain

in no way intersect together.<sup>2,11</sup> Each vortex-core line links one vortex with clockwise rotation of  $\alpha$ ,  $\beta$ , and  $\gamma$  antiphase domains to the corresponding antivortex with anticlockwise rotation of the same antiphase domains. Closed-loop vortices of the 6-fold topology hold the edges of the inmost lenticular FE domain volume which has the same trimerization angle but the displacement of  $R_2$  ions (with the 4b Wyckoff position) and hence FE polarization symmetrical to those of the outer antiphase FE domain that contains the loop. The edges of the four capped volumes of the remaining FE domains with antiphase and polarization directions given by the rules of 6-fold vortices also meet on the closed-loop vortex-core line.<sup>7,10,12,13</sup> The inversion of  $R_2$  ion displacement and hence of electric polarization at APB-FE domain walls in h-RMnO<sub>3</sub> is abrupt and occurs within a single (010)<sub>a</sub> (Type-I APB-FE wall) or double (020)<sub>a</sub> (Type-II) plane spacing taken in the original P6<sub>3</sub>/mmc lattice of the hexagonal apolar h-RMnO<sub>3</sub> phase. The specific surface energy of the APB-FE domain walls is very low and has the lowest estimated values of 10.4 mJ m<sup>-2</sup> and 11.5 mJ m<sup>-2</sup> when they coincide with the {210} and {120} planes of the P6<sub>3</sub>cm h-RMnO<sub>3</sub> lattice, respectively.<sup>3,12</sup> The dimension of the vortex-core diameter has not been established on first principles. But outputs of Monte Carlo simulations, atomic models for local distortion of ion positions where the six APB-FE boundaries in the cover-leaf configuration meet together and direct observation of vortex cores by high-angle annular dark-field (HAADF) in C<sub>s</sub>-corrected STEM microscopy represent the region of intersection of APB-FE interfaces, which are also sharp. It may range from one to two P6<sub>3</sub>cm unit cell sizes or up to five unit cell dimensions if one accounts for the relaxation in the region around vortex-core central lines within the limit of detection of displacements of the R<sup>3+</sup> ions at the frontier of present state-of-the-art electron microscopy. This is also the range of closest distances two APB-FE walls can approach together pressed by the poling of applied electrical fields or by self-poling from gradients of electrochemical potential created at the surfaces of the h-RMnO<sub>3</sub> materials. Such narrow spacing of FE walls and diameters of vortex-cores remain below the best lateral resolution obtained in piezoresponse force microscopy in ambient air.<sup>6,9,14–18</sup>

In the tension field side of the edge dislocation with Burgers vector  $\mathbf{b} = [100]_a$  and {001}<sub>a</sub> slip planes taken in the apolar phase, the slip strain is distributed by elastic deformation at a distance of approximately ten (020)<sub>a</sub> plane spaces, with the slip vector being equivalent to the  $2\pi/3$  phase shift in the trimerization displacement.<sup>7,12,19</sup> The stress field around the edge dislocation is asymmetrical. At the transition temperature T<sub>s</sub> when the polar phase of the h-RMnO<sub>3</sub> phase is formed by trimerization of the apolar phase, the free energy for vortex creation close to the edge dislocation is locally modified and single dislocation truncated-vortices appeared with just the 4-state topology locked to the edge dislocations. If two identical edge dislocations with Burgers vector  $\mathbf{b} = [100]_a$  in neighbor {001}<sub>a</sub> slip planes become associated within a narrow distance comparable to the range of vortex-core diameters, the total Burgers vector given by the accumulated slip strain becomes  $2\mathbf{b} = [200]$  and double-dislocation truncated-vortices with 2-state topology and  $4\pi/3$

trimerization displacement are generated locked to the dislocation pair.<sup>7,17,20</sup> Both dislocations and vortex-core lines can bend inside crystals. Locking vortex-cores to the dislocations of Burgers vector  $\mathbf{b} = [100]_a$  will be lost if the dislocations become mixed or screw dislocations at places where dislocation lines change their orientation. In contrast to 6-fold vortex-core lines, dislocations can react forming nodes of three dislocations composed of poorly organized networks, the Frank net. Rows of dislocations form tilt boundaries and low-angle grain boundaries in bulk materials as well as in flawed single crystals. Fine precipitates pin dislocations and hinder dislocation glides. Post-recoalescence temperature T<sub>p</sub> of rapidly solidified RMnO<sub>3</sub> compounds gives approximate values of their melting points. Values of T<sub>p</sub> have a moderate increase with the Shannon R<sup>3+</sup> ionic radius from T<sub>p</sub> = 1910 K in HoMnO<sub>3</sub> to T<sub>p</sub> = 1960 K in LuMnO<sub>3</sub>.<sup>21</sup> Ductile deformation by creep and activation of primary slip systems of the h-RMnO<sub>3</sub> lattice under applied load were observed in the range of homologous temperatures of 0.72–0.75 of the melting point overlapping with transition temperature, T<sub>s</sub>. The interaction of created vortices with shear strain of the lattice undergoing plastic deformation under load pulls vortices and antivortices in opposite directions moves them in parallel with travelling dislocations gliding in primary slip planes, resulting in long topological stripes closely aligned to slip bands. The interaction of vortex-cores and dislocations represents a complex way of mechanical control of topological defects of the h-RMnO<sub>3</sub> multiferroics. Vortex-cores that otherwise remain immobile for temperatures significantly below T<sub>s</sub> can react to poling with electric fields one order of magnitude above the coercive field or to local heating from lightning discharges at the crystal edges and move towards the edges of the crystal leaving stripe domain patterns behind.<sup>18,22–24</sup>

The temperature of apolar-to-polar phase transition T<sub>s</sub> of h-RMnO<sub>3</sub> is directly proportional to the Shannon R<sup>3+</sup> ionic radius and increases from T<sub>s</sub> = 1373 K in h-HoMnO<sub>3</sub> to T<sub>s</sub> = 1672–1708 K in h-LuMnO<sub>3</sub>, with the value of T<sub>s</sub> for h-YMnO<sub>3</sub> T<sub>s</sub> = 1220–1260 K being roughly 70 K below the corresponding trend value determined from the dependence of T<sub>s</sub> on the ionic radius of the other h-RMnO<sub>3</sub> (R = Ho–Lu) oxides.<sup>5,11,17,25,26</sup> Up to a threshold value of the cooling rate, h-RMnO<sub>3</sub> samples annealed above T<sub>s</sub> and cooled in a controlled way present a density of vortex-core lines (length/volume or intersection points/area) and hence the specific surface area of APB-FE walls and properties they depend which increase in proportion to a non-integer power of the cooling rate. This threshold of the cooling rate that separates the Kibble-Zurek mechanism (low cooling rates) from the anti-Kibble-Zurek regime (at high cooling rates) with the opposite trend moves to higher values with the decrease in the R<sup>3+</sup> ionic radius from Y<sup>3+</sup> to Tm<sup>3+</sup>, implying a large decrease in vortex-core densities for the smaller ionic radius at cooling rates in the range of 1 K min<sup>-1</sup>. The highest values of vortex-core density of the so-called Kosterlitz-Thouless (KT) phase or Higgs phase, in 6-fold topological networks reported for h-RMnO<sub>3</sub> single crystals at the limits of the Kibble-Zurek regime, are around 0.6 vortex  $\mu\text{m}^{-2}$  corresponding to an average vortex-core spacing of 1.35  $\mu\text{m}$ .<sup>5,11,17</sup>

Samples processed or annealed in the narrow temperature range below  $T_s$  develop as equilibrium phase curved loop domains or Coulomb phase, with the annular domain patterns being made of layers of antiphase domains separated by topological APB-FE walls wrapped around the central toroidal volume without a vortex-core. For processing temperatures below 0.95 of  $T_s$ , the Ising-type stripe domain patterns with straight APB-FE walls, which may become curved near the limit of stability of this mechanism, are expected to form as the stable configuration of the APB-FE domains of h-RMnO<sub>3</sub> phases.<sup>11,17</sup> Most of the bulk h-RMnO<sub>3</sub> materials processed by sol-gel methods or by solid-state synthesis from the mixture of oxides, thin films, and even thin plate-like single crystals grown using flux methods were processed at temperatures below the corresponding  $T_s$  temperatures and with cooling rates which are rarely controlled or reported. Adding to the multiplicity of topology patterns of APB-FE domain networks potentiated in the h-RMnO<sub>3</sub> lattices, the fine grain sizes of polycrystalline materials may easily fall below the scale of core-vortex average distances in equilibrium. Due to anisotropy of the APB-FE domain wall, specific surface energy of the FE domain walls of {210} and {120} prismatic planes as well as of the {001} basal planes is the most probable and offers privileged orientations for their observation because they are perpendicular to the image plane when seen in the [100] and [110] zone axis of TEM and STEM microscopy and the former are also normal to the basal {001} planes, and the most extensive face of flux-grown single crystals becomes exposed by selective chemical etching.<sup>7,13,17–19,23,27</sup> Besides extrinsic effects created on FE domain networks by dislocations, defect clusters, and grain boundaries, the random orientation of grains in relation to the surface poses additional complexities in the observation of APB-FE domains of polycrystalline samples. Cutting randomly, the crystalline grains in polished cross-sections of bulk h-RMnO<sub>3</sub> prepared for PFM examination display inclined domain walls in larger proportions than in preferable orientations for their observation with domain walls perpendicular to image planes. Overlapping of FE domains in thin slabs of FE domains of up to 2  $\mu\text{m}$  thickness softens PFM contrast and blurs the traces of sloped domain walls, with the fuzziness being more confusing if occurring near vortex-cores. If such a constraint may easily be lifted in TEM and HAADF/STEM studies of h-RMnO<sub>3</sub> bulk samples by using electron diffraction to find thin sections of grains with correct orientation, in polished cross-sections of polycrystals for PFM examination, the grain orientation can only be determined *ex-situ* by using electron backscatter diffraction (EBSD) in SEM, the spatial resolution of EBSD compared with resolution limits of PFM.<sup>6,14,28,29</sup>

### III. EXPERIMENT

LuMn<sub>x</sub>O<sub>3±δ</sub> ceramics ( $0.92 \leq x \leq 1.12$ ) were prepared by conventional solid state sintering of properly mixed Lu<sub>2</sub>O<sub>3</sub> and MnO<sub>2</sub> oxide powders with a purity of 99.99%. To increase the homogeneity of composition, high temperature annealing in air was performed in three steps; one day firing at each of the isothermal holds 850 °C, 1000 °C, and 1300 °C with intermediary grinding and pressing of samples into

pellets, the time of the last firing step at 1300 °C having been extended to 5 days or 10 days to determine the effect of the annealing time.<sup>30</sup> The grain size and composition change were both checked in SEM/EDS (energy dispersive X-ray spectroscopy). SEM images have shown that by increasing the x value, there is an increase in the grain size from 1.78  $\mu\text{m}$  ( $x = 0.92$ ) to 3.23  $\mu\text{m}$  ( $x = 1.08$ ) for a fixed time of one day annealing. An increase in the grain size is also observed, while the annealing time increases from one day to 10 days, for example, for the  $x = 1.08$  sample, after 10 days of annealing, the grain size reaches an average of 8.1  $\mu\text{m}$ . The change in the volume of the unit cell versus x value shows the sensitivity of the unit cell to the off-stoichiometric in our study (supplementary materials, Fig. A1). A NT-MDT NTEGRA PRIMA modular sensor force microscope was used for AFM/PFM measurements at room temperature in the contact mode (at an AC voltage of 10 V and a frequency of 50 kHz on the tip). Cantilevers purchased from NanoSensor Co., Pointprobe-Plus Silicon-SPM-Sensor made of n<sup>+</sup>-doped silicon coated with Al on the detector side with a tip height of 10–15  $\mu\text{m}$  and a tip radius of 10 nm were used for all measurements. Flat surfaces of the ceramics were prepared by mechanical polishing down to 0.1  $\mu\text{m}$  lapping paper. Polished samples were heated at 130 °C to eliminate surface humidity before PFM experiments. Thin sections for the TEM study were prepared by conventional mechanical polishing and precision ion milling down to electron transparency. A JEOL JEM2200FS FEG 200 kV TEM/STEM equipped with an Omega filter and an EDS-INCA x-sight detector was used for TEM. HRTEM images were energy filtered using a 10 eV energy slit. HAADF-STEM images were taken using a dedicated STEM Hitachi HD2700 equipped with EDS Bruker and nano-diffraction operating at 200 kV.

### IV. RESULTS AND DISCUSSION

Figure 1(a) shows the effect of the annealing time at 1300 °C on evolution of vortices in vacancy-doped samples and in the one of the stoichiometric compositions. The piezoresponse of the two compositions of  $x = 1.08$  (one day annealing, not shown here) and  $x = 1.04$  [10 days of annealing, Fig. 1(a)] reveals the change in the size of 6-fold vortices. Figure 1(b) shows a 6-fold vortex observed in the sample of the stoichiometric composition ( $x = 1.00$ ) annealed for 5 days. In the case of a short annealing time, the ferroelectric domain pattern exhibits a type-II vortex networking with the preferred polarization direction downwards.<sup>2,31</sup> Type-II like vortex patterns are not unique in samples of  $x > 1$ , short annealed, and also, type-I vortex patterns without the dominant polarization direction were observed in the same samples. Vortex pattern dimensions in the sample of  $x = 1.08$ , short time annealing, are roughly below 8  $\mu\text{m}$ . The observation of the wider 6-fold vortex of type-I in Fig. 1(a) with the size close to 20  $\mu\text{m}$  illustrates the effect of the annealing time on the scale of 6-fold vortices. Grain sizes of current ceramics increased with the annealing time, and samples heat treated for a longer time sustain larger FE domains. However, the size of the vortex/anti-vortex shown in Fig. 1(a) goes beyond the estimated grain size in the range of 8 microns for this sample. Within

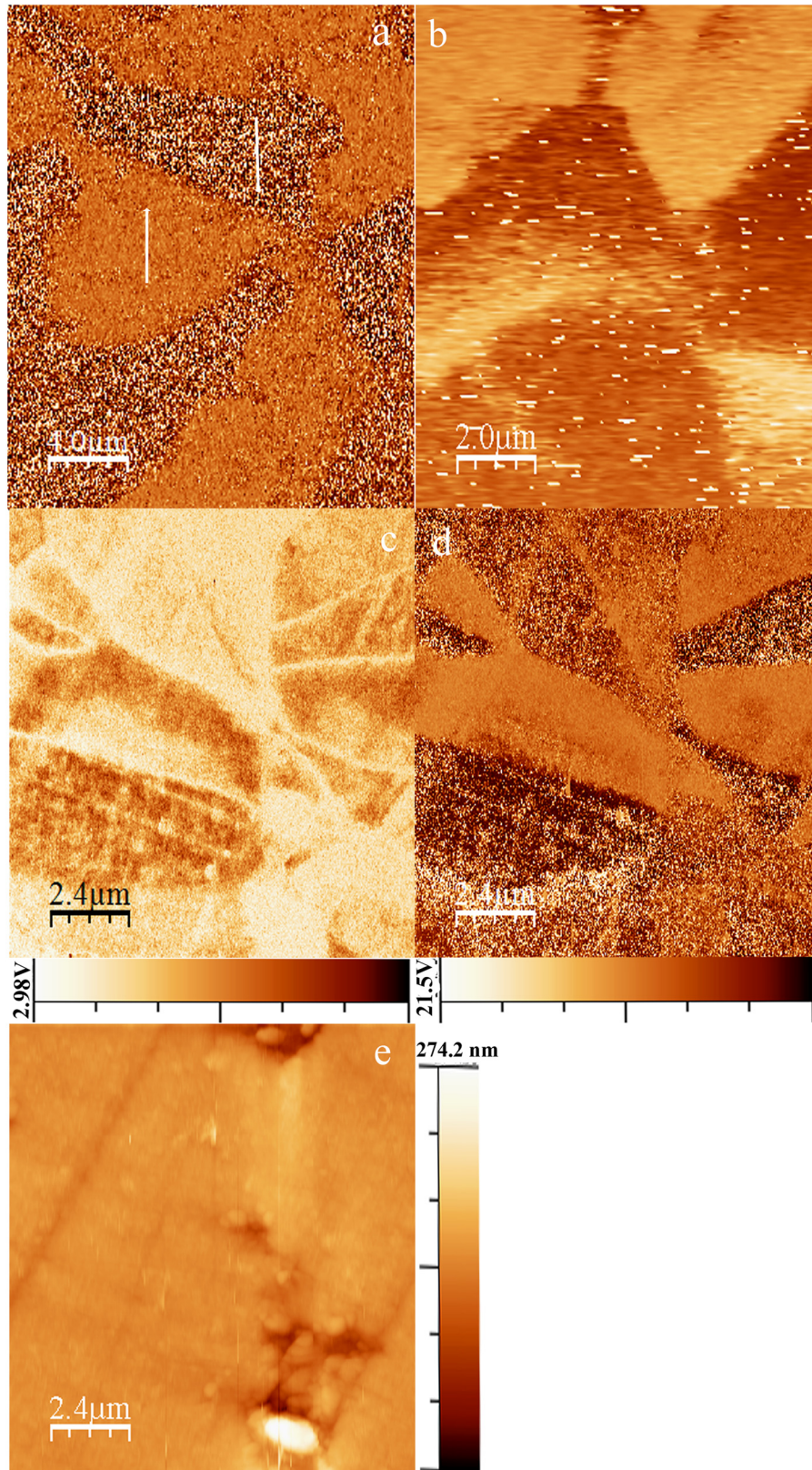


FIG. 1. (a) PFM image of 6-fold vortices in the  $x = 1.04$  sample (10 days of annealing) and  $20 \mu\text{m}$  wide. (b) PFM image of 6-fold vortices of the  $x = 1.00$  stoichiometric sample after 5 days of annealing with a size less than  $10 \mu\text{m}$ . The topography map of figures (a) and (b) is provided in the [supplementary materials](#), Fig. A2. FE domains of the  $x = 0.92$  sample (10 days of annealing), (c) amplitude map, and (d) phase map, where the left side of the images shows 6-fold vortices and the right side broken 6-fold symmetry upon meeting the grain boundary. (e) The topography map of (c) and (d).

the resolution limit of PFM apparatus, vortex core fragmentation of 6-fold vortices is found, which had been shown to be a feature of vortex patterns in either a-c or b-c planes of the hexagonal lattice.<sup>1,13</sup> Core fragmentation in h-YbMnO<sub>3</sub> single crystals was discussed because the presence of the same trimerization antiphase resulted in the existence of charged

head-to-head domain walls of high energy, while in the present case, the phase map in the area of the bulk material analyzed by PFM is incomplete and insufficient to indicate head-to-head domain walls in Fig. 1(b).<sup>31</sup>

Figure 1(c) displays FE domains of the  $x = 0.92$  sample after a long annealing time (10 days). The left part of

Fig. 1(c) shows 6-fold vortices where upward polarization (bright region) occupies lesser area than regions of downward polarization. Non-uniform distributions of upwards and downwards polarized FE domains give rise to type-II vortex patterns.<sup>31</sup> Present investigation of samples with either Mn vacancies or Lu vacancies and the stoichiometric composition annealed for different times could only find 6-fold vortices of type-I in samples with  $x \geq 1$ . Introducing Mn vacancies ( $x < 1$ ) likely changed the type of FE domain network to the type-II pattern regardless of how long annealing takes place. Three stripe-like FE domains with alternation of polarization and phase are observed in the right part of Figs. 1(c) and 1(d), while their propagation cannot be continued further. The topography map of the same region revealed that the spread of topological defects is interrupted at the grain boundaries. Elongation of the three FE domains observed in this figure does not replicate the geometry of 6-fold symmetry of FE domains, showing type II FE walls. Breaking of 6-fold symmetry driven by the chemical composition of the gaseous atmosphere was reported in Ar-grown (oxygen deficient) single crystal YMnO<sub>3- $\delta$</sub> , whereas the air-grown single crystal retains the regular topology of the FE domains.<sup>32,33</sup> Type-II domain walls were found near the free surface of h-RMnO<sub>3</sub> single crystals after electrical poling with applied electrical fields or due to self-poling by the electrical field component of total electrochemical potential that drives interdiffusion of ionic species at high temperature resulting from shifts of oxygen activity in the atmosphere.<sup>2,31</sup> In samples with a nominal concentration of 0.08% Mn vacancies, the shift in the chemical composition can be considered as the most probable reason for promoting the appearance of stripe-like FE domains.

Grain boundaries and pores shall affect the mechanisms of FE domain growth in bulk ceramic materials. Their effects had not been comprehensively studied in h-RMnO<sub>3</sub> oxides, yet. The white circle in the right of Fig. 2(a) indicates the position of the triple line where grain boundaries met [the topography map of the same region is provided in Fig. 2(c)]. The local curvature of the grain boundaries is determined by the equilibrium of surface tension forces. Figure 2(a) shows a second example of FE domains in broken 6-fold symmetry, where three of the FE domains with opposite polarization directions and different phases emerge from the clamping point on the wall of a large FE domain in the neighbor crystalline grain (the black dashed line). The three FE domains creating the truncated vortex in Fig. 2(a) belong to the same crystalline grain of the bulk ceramics (more figures of the same region are given in the [supplementary materials](#), Fig. A3). The formation of a complete 6-fold vortex was hampered upon meeting the grain boundary (indicated by the black dashed line). Missing 6-fold symmetry of the vortex is also observed in the stoichiometric sample ( $x = 1.00$ , 5 days of annealing) in Fig. 2(b) inside a large grain where the topology map ensures the absence of grain boundaries. Vanishing of one FE domain in neighboring FE domains of opposite polarization is seen on the left, down part of Fig. 2(b) where a 6-fold vortex would be expected. The inset of Fig. 2(b) shows the smoothed profile intensity of voltage taken across the marked line in the same figure. The

topography map of the same region is shown in Fig. 2(d). The intensity profile in the phase map and in the amplitude map (not shown) reveals the trace of the fading FE domain with downward polarization limited by faint walls in a narrow width of about 300 nm. Compared to oxygen deficient crystals, Fig. 2(b) does not present type-II FE domain or atypical domain patterns of vacancy doped h-RMnO<sub>3</sub> single crystals. Instead, weakening of the downward FE domain can be assigned to canting of the vortex core with inclined domain walls or to dislocations in the lattice to be discussed later.

Figure 2(e) and d reveal the dispersion of nano-sized FE domains inside wider domains with opposite polarization. This scenario of dispersive nano-regions possessing different phase shifts or polarization directions from the parent FE domain surrounding them was also observed in samples of other compositions in this study. Upward polarization (bright regions) is dominant in a wide extension displayed in Fig. 2(e), whereas regions of downward polarization form discrete patches. From the region of downward polarization in the inset of Fig. 2(e), the image of higher magnification in Fig. 2(f) clearly confirms the presence of nano-FE domains inside larger FE domains with opposite polarization.

To shed light on the interaction of FE domains of self-doped ceramics and the applied electric field, PFM images were taken before and after electrical poling of the region shown in Fig. 3(a) of the  $x = 1.04$  sample (10 days of annealing). Figure 3(a) presents a set of narrow FE domains of negative (darker contrast) and positive (brighter contrast) polarization. Poling was done by applying an external potential of +30 V on the region shown in Fig. 3(b) where a narrow negative domain is surrounded by two domains of positive polarization. As clearly seen in Fig. 3(c) of the poled area, the applied field increased the width of the negative domain and diffused the domain walls. The reversibility of the FE domain was tested by applying a negative voltage (-30 V) on the same region. The original FE configuration of Fig. 3(b) before the poling experiment is reproduced back in Fig. 3(d) after reverse poling although the contrast is slightly changed. Profiles of PFM response intensity along the arrow lines before poling and after successive poling experiments are compared in the inset of Fig. 3(d). Width broadening of the negative domain from the profile after +30 V poling and almost complete recovery of the negative domain after -30 V poling are visible. Positive poling reduces the intensity of positive domains, whereas the intensity of the negative domain under positive or negative poling remains the same as before poling. This experiment and similar experiments on other samples show pinning of negative domains upon applying a positive field which is restored by changing the polarization of the electrical field. Restoring of the original polarization of the FE domains after poling shown in Fig. 3 indicates that the memory effect of FE domains exists in self-doped h-RMnO<sub>3</sub> ceramics.

Electron microscopy analysis of defective regions was performed to characterize the interactions of defects and ferroelectricity in the lattice of h-RMnO<sub>3</sub> ceramics. The high magnification DF-TEM image in Fig. 4(a) shows the complete 6-fold vortex pattern of size in the range of 150 nm with the indication of the phase shift and polarization of the

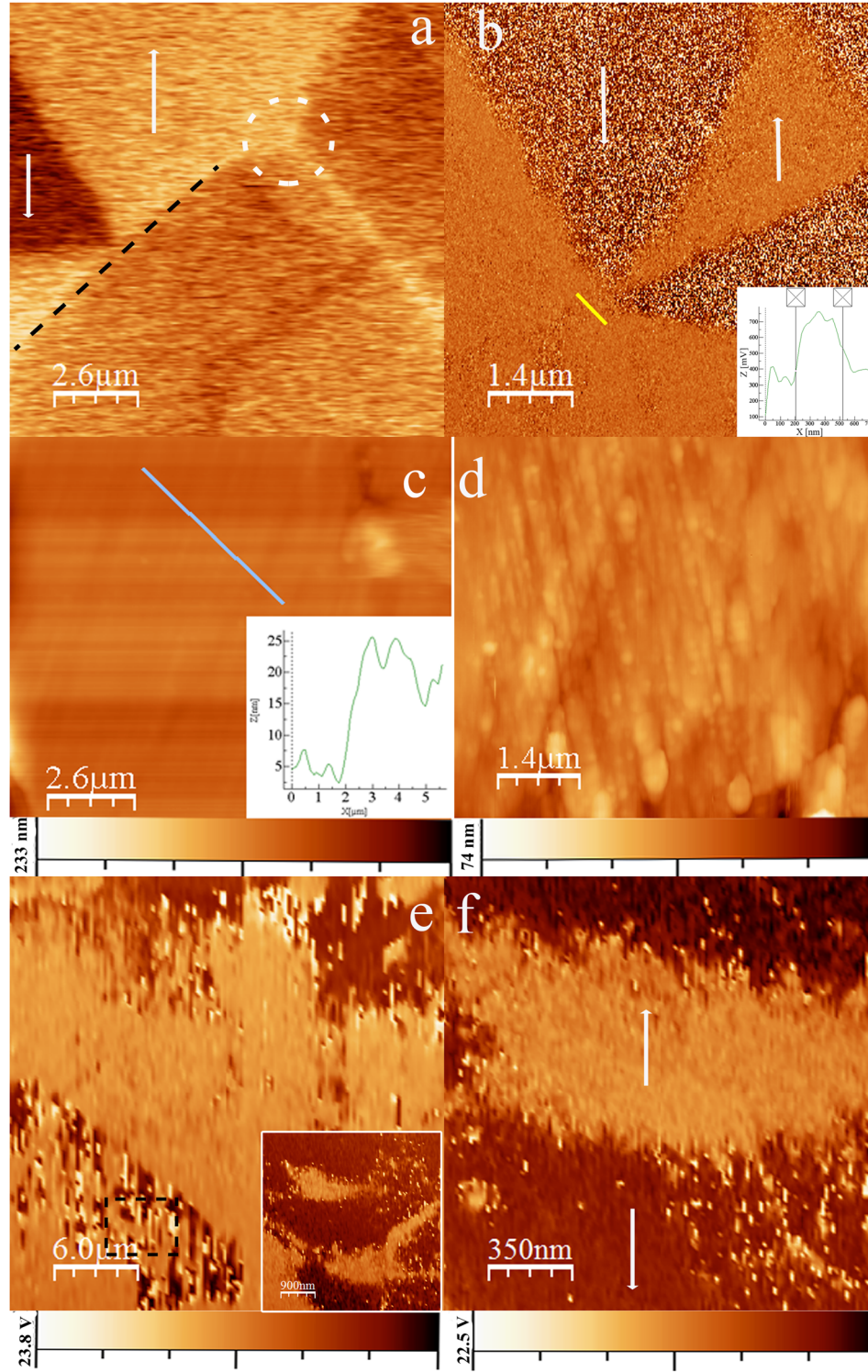


FIG. 2. (a) and (c) Phase and topography maps of a broken 6-fold symmetry of the  $x = 1.04$  sample (5 days of annealing), the dark-dashed line shows the grain border where topology breaking occurs, and the white circle shows the triple line of three grain-boundaries. The light, blue line in (c) shows the location of the grain boundary, whereas the inset in the image shows the change in the height profile indicating the sudden step. (b) and (d) Phase and topography maps of topology breaking in the  $x = 1.00$  sample (5 days of annealing) where missing of one of the FE domains with downward polarization is noted; variation in voltage across the yellow line is given in the inset, and the distance between two markers is 290 nm. (e) Large FE domain with upward polarization seen in the  $x = 1.04$  sample (10 days of annealing), revealing dispersed FE nano-domains of opposite polarization, with the black-dashed box illustrating the part of the image shown in the inset; (f) enlarged image of the inset in (e), confirming the existence of nano-FE domains in image (e) (Fig. A4 in the [supplementary materials](#) show additional analysis of the same region).

FE domains found in the  $x = 1.04$  sample on the edge of the particle in the inset of Fig. 4(b). Figure 4(b) shows the HAADF-STEM image of this particle in the right side of the vortex. The displacement of the Lu ions as two up one down corresponds to upward polarization of the FE domain. The nano-vortex is located at the end of a planar defect, with the defect being extended to the inside of the particle. The planar defect splits into two branches near the edge of the particle at a distance roughly 200 nm away from the vortex core. The DF-TEM image of the planar defect in the inset of

Fig. 4(b) was taken by selecting the 004 diffraction spot with the particle aligned to the  $\langle 110 \rangle$  zone axis. EDS analysis did not reveal any change in the composition on scanning domain walls between FE domains.

The STEM image of two planar defects converging to the point on the edge of a second particle of the same sample is shown in Fig. 5(a). In the inset of Fig. 5(a), the EDS analysis across one of the planar defects, marked with the arrow, shows the deviation of the  $x = \text{Mn/Lu}$  ratio from the  $x = 1.08$  average composition on crossing the defective region. To

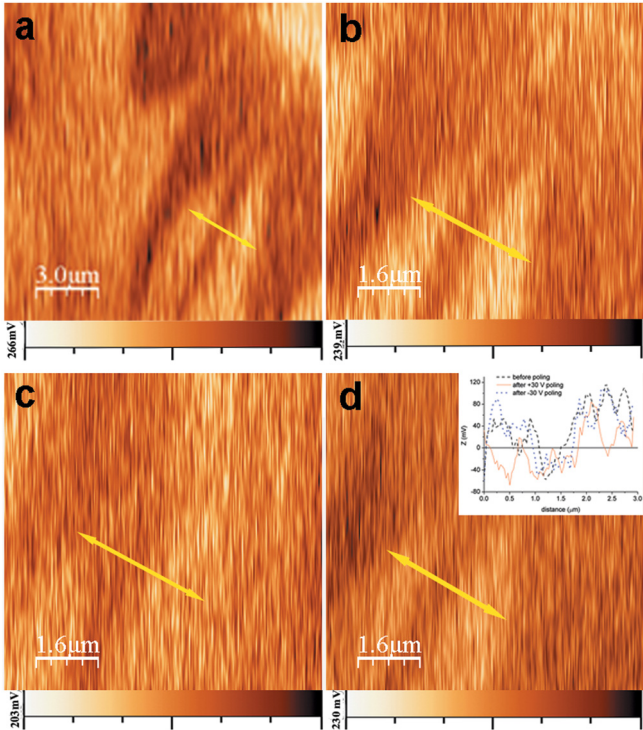


FIG. 3. (a). PFM image of the  $x = 1.04$  sample (10 days of annealing), showing FE domains of negative (dark contrast) and positive (bright contrast) polarization. (b) Area selected for the electrical poling experiment, (c) after applying a poling voltage of  $+30$  V and (d) after applying a voltage of  $-30$  V, showing the same FE domain initially seen in Fig. 3(b). The inset shows the intensity profile of the voltage across the arrowed lines before and after poling.

exclude the contribution of copper from the sample holder in the EDS analysis, the Mn/Lu ratio was calculated from the intensities of  $K_{\alpha 1}$  of the Mn line and  $L_{\alpha 1}$  of the Lu line. The HRTEM image of the lattice around the planar defect with the particle aligned to the  $\langle 110 \rangle$  zone axis in Fig. 5(b) exhibits changes in the structure of the lattice, revealing the presence of one anti-phase boundary marked by two yellow

lines. One cannot determine polarization switching across the planar defect. Interference of extended defects of the crystal with topological defects can affect the appearance of 6-fold vortices, giving rise to vortices with even sub-six topological orders.<sup>7,8</sup>

Switching of FE polarization near an extended defect is seen in the TEM image along the  $[110]$  zone axis of the  $x = 1.00$  sample (5 days of annealing) in Fig. 5(c) where the contrast and profiles of intensity are used to pin point the planes of the APB-FE domain walls with switching of the phase of the Lu ion displacement. The same criteria were used to determine the phase shift of the two neighboring FE domains.<sup>2,7</sup> The inset of Fig. 5(c) displays the low magnification TEM image of the defective region and lattice around it. Lines 1 and 2 in Fig. 5(c) show Lu rows under the influence of the defect. Intensity profiles were determined along these lines, plots in Fig. 5(d), with contrast heights indicating the position and displacements of Lu ions. The sharp switching of the polarization pitch in the intensity profiles gives the position and type of APB-FE wall. Both APB-FE walls crossed by lines 1 and 2 are of type-II with one apolar ion plane separating antiphase FE domains of opposite polarity, respectively. The appearance of the APB-FE domain walls seems to emerge from the strain field created in the lattice by the defect. The strain/stress effect on topological defects in single crystals of h-ErMnO<sub>3</sub> was recently investigated.<sup>7,8,23</sup> Shear strain of applied loads on the h-RMnO<sub>3</sub> crystals at high temperature forces the movement of vortices along the planes of the maximum shear strain rate with anti-vortices moving in the opposite direction to the corresponding vortices. By the effect of coordinated movements, the FE domains are stretched to topological stripes with FE domain walls preferentially aligned along the primary slip planes, the  $\{110\}$  planes of the hexagonal lattice.<sup>23</sup> The lattice may show changes in the FE wall type in the transition region from the 6-fold vortices to stretched-stripe FE domains.<sup>23</sup> The interaction of topological defects with extended defects, namely, the partial edge

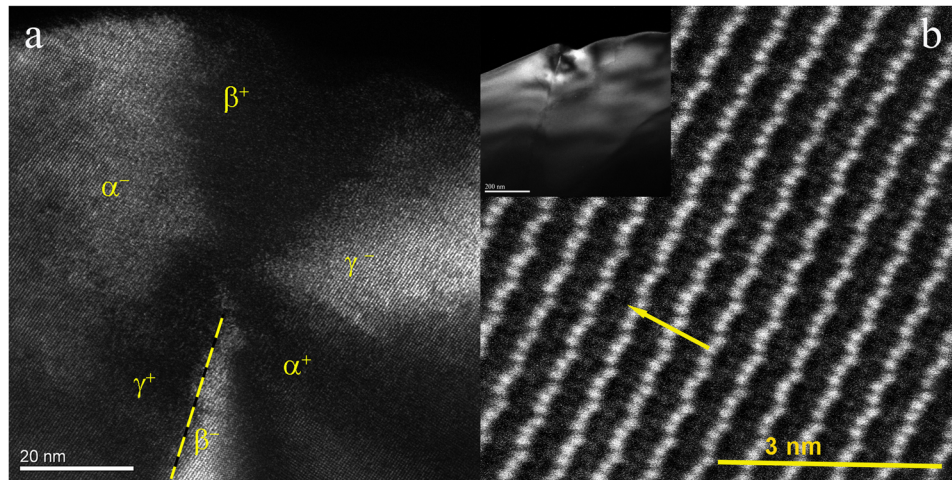


FIG. 4. (a) DF-TEM image of the crystalline grain of the  $x = 1.04$  sample (10 days of annealing) aligned to the  $\langle 110 \rangle$  zone axis with a 6-fold vortex of nanodimensions on the edge of the particle, with the antiphase shift of FE domains. The dashed line shows the approximate location of the planar defect propagated into the vortex-core. The (004) plane of the diffraction pattern was used to take dark field images. (b) The HAADF-STEM image of the same lattice area of (a), showing the electrical polarization direction (the arrow) corresponding to the displacement of the Lu ions; inset: low magnification TEM dark field image of the same area of the crystalline grain with an extended planar defect propagated from the edge to the inside of the particle.

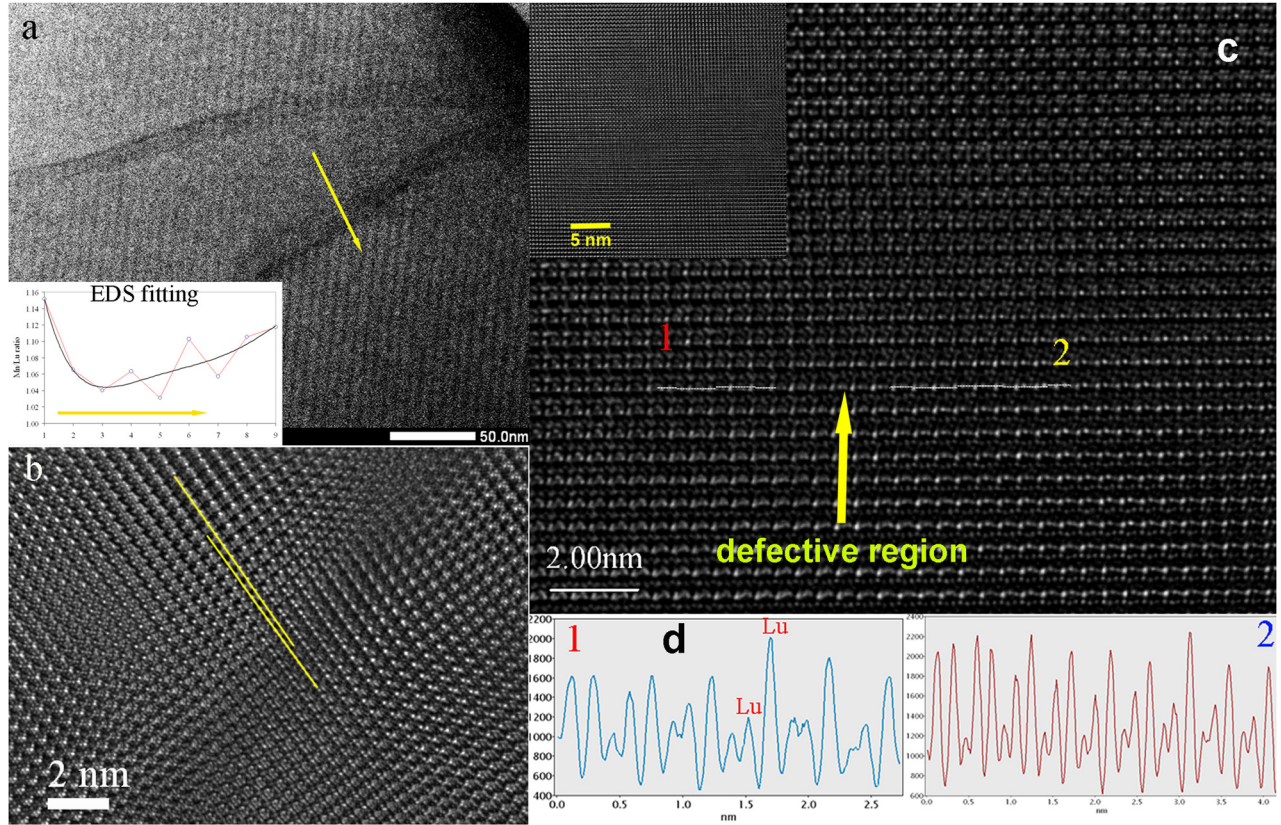


FIG. 5. (a)  $x = 1.04$  sample (10 days of annealing), aligned to the  $\langle 110 \rangle$  zone axis, and two planar defects emerging from the same core upon EDS analysis across the defects are shown in the inset. (b) HRTEM image of the same region taken from one of the planar defects, displaying the anti-phase boundary like structure. (c) HRTEM image of the  $x = 1.00$  sample (5 days of annealing); arrangements of Lu ions around a defect are shown in the inset of (c), and the white lines marked 1 and 2 were used to determine the profile intensities used to identify the position of atomic planes with FE switching and antiphase shifts on the domain wall in (d).

dislocations in  $\text{Y}_{0.67}\text{Lu}_{0.33}\text{MnO}_3$  (Ref. 7) or  $\text{YMnO}_3$  (Ref. 8) single crystals, generated unconventional features of FE vortices, namely, low even order vortices: 4-fold vortex or single dislocation truncated vortex and 2-fold vortex or a double dislocation truncated vortex. As shown in Fig. 5(c), nano-regions of opposite polarization and different phases are formed where extended defects are present. Extended planar defects of large dimensions like those displayed in Figs. 4(a) and 5(a) can duly modify the propagation of symmetric 6-fold vortices. In view of the PFM image in Fig. 2(b), narrowing or extinction of one of the FE domains out of the set in 6-fold vortices would then result.

Strain fields in the lattice change the energy scheme of FE domain walls and cores of vortices. Core fragmentation is assisted by the repulsive potential of the FE domains of the same type.<sup>31</sup> Detailed inspection of Fig. 4(b) of Ref. 23 taken from one h- $\text{ErMnO}_3$  single crystal under mechanical loading during thermal treatment at 10 K above  $T_C$  and a controlled cooling rate reveals the emergence of FE domains in aligned anti-vortices and patterns of surface poling at the ends of the topological stripes at the edge of the single crystal.<sup>23</sup> The absence of convergence of FE domains in 6-fold vortices to a central point is not rare in h- $\text{RMnO}_3$  materials, and single crystals of  $\text{YMnO}_3$  often reveal core fragmentation.<sup>8,12,19</sup> The same scenario seems to be repeated in ceramics of h- $\text{LuMnO}_3$  in Fig. 4(a). Core fragmentation in the 6-fold vortex of the DF-TEM image in Fig. 4(a) occurs where the planar defect

crosses the core of the topological vortex. The PFM image in Fig. 1(b) also points to core fragmentation of 6-fold FE vortices of wider scales. Based on the TEM observation, core fragmentation can originate from strain fields in the lattice induced by planar defects. Besides core fragmentation, the presence of one type of FE domain,  $\beta^-$ , right on the planar defect in Fig. 4(a) and switching of polarization across the defect strikingly display pinning of FE domains to planar defects. In their nature, topological defects in h- $\text{RMnO}_3$  oxides come from interlocking of FE domain walls and the anti-phase domain walls within less than a unit cell width.<sup>2</sup> Figure 4(a) shows in another aspect the interaction of ferroelectricity and defects with broader domain walls.

The existence of planar defects accompanied by shifts in the chemical composition was reported in h- $\text{RMnO}_3$  single crystals when oxygen vacancies were present.<sup>22,31,32,34</sup> For the case of the sample in Fig. 5, the defective region of the crystalline lattice appears to be associated with local fluctuations in the composition. Analogous observation nearby planar defects was done in the  $x = 0.92$  sample. Selected area electron diffraction (SAED) patterns in defective regions may be sensitive enough to detect oxygen vacancy ordering in the crystalline structure of h- $\text{RMnO}_3$  oxides.<sup>35,36</sup> Fe-doped  $\text{YMnO}_3$  (Ref. 37) and  $\text{In}_x\text{Ga}_{1-x}\text{MnO}_3$  (Ref. 38) revealed quite complex images of topological defects compared to those reported for the pure compounds. Ti-doping of  $\text{YMnO}_3$  also changed the formation of topological defects in single crystals.<sup>39</sup> Type-II FE domain

networks were reported to be more sensitive than type-I domain networks to the chemical gradients in the composition like those described in crystalline lattices self-poled by oxygen vacancy gradients.<sup>31,40</sup> The chemical inhomogeneity of the lattice of h-LuMn<sub>x</sub>O<sub>3±δ</sub> bulk ceramics gave rise to new features in topological defects. The hypothetical presence of oxygen vacancies was investigated by looking for the absence of (111) and (222) diffraction spots as an indicator of oxygen vacancy ordering. The search in large scale SAED patterns in self-doped h-LuMn<sub>x</sub>O<sub>3±δ</sub> samples of this study gave no evidence of the absence of these diffraction spots neither the FFT nor HRTEM images taken from some of the samples provided indication of ordering of oxygen vacancies in the lattice. On the basis of this analysis, one cannot establish that oxygen off-stoichiometry if present in vacancy doped h-LuMn<sub>x</sub>O<sub>3±δ</sub> oxide has concentration high enough to create long range oxygen vacancy ordering of point defects at a detectable threshold in the crystalline structure. Coupling of shifts in the chemical composition and planar defects to the formation of FE domains must be considered. In support of this, the PFM analysis in Fig. 1(b) and c of the x = 0.92 sample with a highly defective lattice revealed only atypical domain shapes far from those of APB-FE domains in topological type-I or type-II domain networks of the h-RMnO<sub>3</sub> single crystals.

Condensation and annihilation of FE domain walls in h-LuMnO<sub>3</sub> single crystals at different cooling rates were recently discussed.<sup>17</sup> It was shown that cooling of LuMnO<sub>3</sub> through T<sub>C</sub> (1672 K) resulted in the formation of 6-fold vortices, with the density of vortices in the h-RMnO<sub>3</sub> being dependent on the cooling rate and R ionic radius.<sup>5,9,17</sup> Heat treatment below T<sub>C</sub>, e.g., 1671 K or 1593 K, followed by controlled rate cooling yielded close-loop, annular domain or straight-stripe domain patterns, respectively, with annihilation of vortex/anti-vortex patterns being observed.<sup>17</sup> Sintering followed by long time annealing at a constant temperature of LuMn<sub>x</sub>O<sub>3</sub> ceramics in the present study was done at 1573 K, 100 K below the value of T<sub>C</sub> reported above. At the comparatively low process temperature of 94% of T<sub>C</sub> of LuMnO<sub>3</sub>, low density straight-stripe patterns would be expected in the crystalline grains of the bulk ceramic. The current investigation on self-doping of h-RMn<sub>x</sub>O<sub>3</sub> ceramics indicates that dealing with ceramics where grain boundaries and planar defects play key roles in properties, the condensation and annihilation mechanism of FE vortex/antivortex patterns needs to be reexamined. Keeping constant the cooling rate for LuMn<sub>x</sub>O<sub>3</sub> bulk materials processed below T<sub>C</sub>, one observed vortex/antivortex patterns in these ceramics where only the nominal vacancy contents and annealing time were variables. The microstructural study of the same samples has proven that these two parameters are major factors governing the final grain size and overall quality of LuMn<sub>x</sub>O<sub>3</sub> ceramics. The main driving force for the creation of vortices below T<sub>C</sub> has to be looked for fluctuations in chemical potential during growth of grains. This hypothesis can be linked to the observation of FE vortices/circles in synthesized YMnO<sub>3</sub> and YMn<sub>0.9</sub>Fe<sub>0.1</sub>O<sub>3</sub> particles below T<sub>C</sub>.<sup>37</sup> The matter of condensation/annihilation of vortex/antivortex upon cooling above or below T<sub>C</sub> in bulk RMnO<sub>3</sub> ceramics deserves further study. The role of chemical shifts in the lattice in the creation of

different patterns of FE domains like vortices, stripes, or circular domains below T<sub>C</sub> should be further examined in single crystals of h-RMnO<sub>3</sub> oxides whenever off-stoichiometric on either the Mn site or the rare-earth site is introduced.

FE domains and topological defects in h-LuMn<sub>x</sub>O<sub>3±δ</sub> bulk ceramics with the lattice altered by the Mn/Lu ratio were investigated here. Patterns of complete 6-fold vortices in different sizes were found upon changing the annealing time or introducing Lu vacancies. It is found that Lu vacancy doping led to large FE domains as fast grain growth on the x > 1.00 side of the h-LuMn<sub>x</sub>O<sub>3±δ</sub> solid solution yields dense microstructures with coarse grain sizes. Large 6-fold vortices of size as large as 20 μm comparable to those found in single crystals could be replicated by h-LuMn<sub>x</sub>O<sub>3±δ</sub> ceramics via Lu vacancy doping and enlarging the grain size by increasing the annealing time at 1300 °C. Grain boundaries and planar defects inside crystalline grains were identified as common 6-fold vortex topology breaking features. Nano-vortices were revealed by TEM microscopy where pinning of FE domains to planar defects was observed. FE polarization switching determined in HRTEM images reveals that planar defects or chemical inhomogeneity inside crystalline grains play a major role in ferroelectricity. SAED patterns of electron diffraction fail to substantiate oxygen vacancy ordering in the crystalline lattice of self-doped samples although the FE domain network was observed in PFM images of Mn vacancy doped samples. Poling followed by reversed poling showed that the memory effect exists for the FE domains in off-stoichiometric ceramics of the h-LuMn<sub>x</sub>O<sub>3±δ</sub> solid solution.

## SUPPLEMENTARY MATERIALS

See [supplementary material](#) for the change in the volume of the unit cell of sintered ceramics versus x at different annealing times (Fig. A1) and complementary AFM and PFM images of some figures discussed in the text (Figs. A2, A3, and A4), as were addressed in the text.

## ACKNOWLEDGMENTS

A.B. would like to acknowledge the financial support of FCT fellowships SFRH/BD/51140/2010. We would like to acknowledge the Electron Microscopy Group in Fritz Habor Institute, Berlin, for providing the Equipment for TEM Studies. A.B acknowledges Achim Klein-Hoffmann for teaching sample preparation and his support. Also, we would like to acknowledge the help of staff in the Microscopy Center of the Aveiro University, Portugal, and the FCT Project No. REDE/1509/RME/2005 for providing access to electron microscopy facilities in CICECO and also PFM equipment in CICECO.

<sup>1</sup>D. Meier, M. Lilienblum, P. Becker, L. Bohaty, N. A. Spaldin, R. Ramesh, M. Fiebig, and L. Bohatý, *Phase Trans.* **86**, 33 (2013).

<sup>2</sup>S. Chae, Y. Horibe, D. Jeong, N. Lee, K. Iida, M. Tanimura, and S.-W. Cheong, *Phys. Rev. Lett.* **110**, 167601 (2013).

<sup>3</sup>Y. Kumagai and N. A. Spaldin, *Nat. Commun.* **4**, 1540 (2013).

<sup>4</sup>H. Das, A. L. Wysocki, Y. Geng, W. Wu, and C. J. Fennie, *Nat. Commun.* **5**, 2998 (2014).

<sup>5</sup>S. M. Griffin, M. Lilienblum, K. T. Delaney, Y. Kumagai, M. Fiebig, and N. A. Spaldin, *Phys. Rev. X* **2**, 041022 (2012).

- <sup>6</sup>J. Li, F.-K. Chiang, Z. Chen, C. Ma, M.-W. Chu, C.-H. Chen, H. Tian, H. Yang, and J. Li, *Sci. Rep.* **6**, 28047 (2016).
- <sup>7</sup>Q.-H. Zhang, G.-T. Tan, L. Gu, Y. Yao, C.-Q. Jin, Y.-G. Wang, X.-F. Duan, and R.-C. Yu, *Appl. Phys. Lett.* **105**, 12902 (2014).
- <sup>8</sup>L. Tian, Y. Wang, B. Ge, X. Zhang, and Z. Zhang, *Appl. Phys. Lett.* **106**, 112903 (2015).
- <sup>9</sup>M. Lilienblum, T. Lottermoser, S. Manz, S. M. Selbach, A. Cano, and M. Fiebig, *Nat. Phys.* **11**, 1070 (2015).
- <sup>10</sup>S. Artyukhin, K. T. Delaney, N. A. Spaldin, and M. Mostovoy, *Nat. Mater.* **13**, 42 (2014).
- <sup>11</sup>S. C. Chae, N. Lee, Y. Horibe, M. Tanimura, S. Mori, B. Gao, S. Carr, and S.-W. W. Cheong, *Phys. Rev. Lett.* **108**, 167603 (2012).
- <sup>12</sup>T. Jungk, Á. Hoffmann, M. Fiebig, E. Soergel, A. Hoffmann, M. Fiebig, and E. Soergel, *Appl. Phys. Lett.* **97**, 12904 (2010).
- <sup>13</sup>B. Mettout, P. Tolédano, M. Lilienblum, and M. Fiebig, *Phys. Rev. B* **89**, 24103 (2014).
- <sup>14</sup>T. Jungk, Á. Hoffmann, and E. Soergel, *New J. Phys.* **10**, 13019 (2008).
- <sup>15</sup>B. J. Rodriguez, S. Jesse, A. P. Baddorf, and S. V. Kalinin, *Phys. Rev. Lett.* **96**, 237602 (2006).
- <sup>16</sup>T. Choi, Y. Horibe, H. T. Yi, Y. J. Choi, W. Wu, and S.-W. Cheong, *Nat. Mater.* **9**, 253 (2010).
- <sup>17</sup>S.-Z. Lin, X. Wang, Y. Kamiya, G.-W. Chern, F. Fan, D. Fan, B. Casas, Y. Liu, V. Kiryukhin, W. H. Zurek, C. D. Batista, and S.-W. Cheong, *Nat. Phys.* **10**, 970 (2014).
- <sup>18</sup>Q. Zhang, G. Tan, L. Gu, Y. Yao, C. Jin, Y. Wang, X. Duan, and R. Yu, *Sci. Rep.* **3**, 2741 (2013).
- <sup>19</sup>Y. Yu, X. Zhang, Y. G. Zhao, N. Jiang, R. Yu, J. W. Wang, C. Fan, X. F. Sun, and J. Zhu, *Appl. Phys. Lett.* **103**, 32901 (2013).
- <sup>20</sup>A. del Campo, A. Retzker, and M. B. Plenio, *New J. Phys.* **13**, 83022 (2011).
- <sup>21</sup>M. S. Vijaya Kumar, N. Higaki, K. Kurabayashi, T. Hibiya, and S. Yoda, *J. Am. Ceram. Soc.* **94**, 281 (2011).
- <sup>22</sup>S. C. Chae, Y. Horibe, D. Y. Jeong, S. Rodan, N. Lee, and S.-W. Cheong, *Proc. Natl. Acad. Sci. U.S.A.* **107**, 21366 (2010).
- <sup>23</sup>X. Wang, M. Mostovoy, M. G. Han, Y. Horibe, T. Aoki, Y. Zhu, and S.-W. Cheong, *Phys. Rev. Lett.* **112**, 247601 (2014).
- <sup>24</sup>D. Hull and D. J. Bacon, *Introduction to Dislocations* (Butterworth-Heinemann, 2011).
- <sup>25</sup>T. Lonkai, D. G. Tomuta, U. Amann, J. Ihringer, R. W. A. Hendrikx, D. Többens, J. A. Mydosh, D. M. Tobbens, and J. A. Mydosh, *Phys. Rev. B - Condens. Matter Mater. Phys.* **69**, 134108 (2004).
- <sup>26</sup>H. Sim, J. Oh, J. Jeong, M. D. Le, and J. G. Park, *Acta Crystallogr., Sect. B* **72**, 3 (2016).
- <sup>27</sup>T. Katsufuji, S. Mori, M. Masaki, Y. Moritomo, N. Yamamoto, and H. Takagi, *Phys. Rev. B* **64**, 104419 (2001).
- <sup>28</sup>M. Lilienblum, E. Soergel, and M. Fiebig, *J. Appl. Phys.* **110**, 52007 (2011).
- <sup>29</sup>B. A. Almeida, M. C. Ferro, A. Ravaner, P. M. F. Grave, H.-Y. Wu, M.-X. Gao, Y. Pan, F. J. Oliveira, A. B. Lopes, and J. M. Vieira, *IOP Conf. Ser. Mater. Sci. Eng.* **55**, 12001 (2014).
- <sup>30</sup>A. Baghizadeh, J. M. Vieira, J. S. Amaral, M. P. Graça, M. R. Soares, D. A. Mota, and V. S. Amaral, *J. Magn. Magn. Mater.* **395**, 303 (2015).
- <sup>31</sup>X. Wang, F.-T. Huang, R. Hu, F. Fan, and S. Cheong, *APL Mater.* **3**, 41505 (2015).
- <sup>32</sup>Y. Du, X. Wang, D. Chen, Y. Yu, W. Hao, Z. Cheng, and S. X. Dou, *Phys. Chem. Chem. Phys.* **15**, 20010 (2013).
- <sup>33</sup>Y. Du, X. L. Wang, D. P. Chen, S. X. Dou, Z. X. Cheng, M. Higgins, G. Wallace, and J. Y. Wang, *Appl. Phys. Lett.* **99**, 252107 (2011).
- <sup>34</sup>D. P. Chen, Y. Du, X. L. Wang, Z. X. Cheng, S. X. Dou, Z. W. Lin, J. G. Zhu, and B. Xu, *J. Appl. Phys.* **111**, 07D913 (2012).
- <sup>35</sup>S. Cheng, S. Q. Deng, Y. G. Zhao, X. F. Sun, and J. Zhu, *Appl. Phys. Lett.* **106**, 62905 (2015).
- <sup>36</sup>Q. H. Zhang, X. Shen, Y. Yao, Y. G. Wang, C. Q. Jin, and R. C. Yu, *J. Alloys Compd.* **648**, 253 (2015).
- <sup>37</sup>M. H. Harunsani, J. Q. Li, Y. B. Qin, H. T. Tian, J. Q. Li, H. X. Yang, and R. I. Walton, *Appl. Phys. Lett.* **107**, 62905 (2015).
- <sup>38</sup>F.-T. Huang, X. Wang, S. M. Griffin, Y. Kumagai, O. Gindele, M.-W. Chu, Y. Horibe, N. A. Spaldin, and S.-W. Cheong, *Phys. Rev. Lett.* **113**, 267602 (2014).
- <sup>39</sup>S. Mori, K. Kurushima, H. Kamo, Y. Ishii, F.-T. Huang, Y. Horibe, T. Kastufuji, and S.-W. Cheong, *Ferroelectrics* **462**, 50 (2014).
- <sup>40</sup>F. Xue, X. Wang, I. Socolenco, Y. Gu, L.-Q. Chen, and S.-W. Cheong, *Sci. Rep.* **5**, 17057 (2015).